Monthly Notices
of the
ROYAL ASTRONOMICAL SOCIETY

MNRAS **511,** 1336–1348 (2022)
Advance Access publication 2022 January 13

https://doi.org/10.1093/mnras/stac084

Particle acceleration and multimessenger emission from starburst-driven galactic winds

Enrico Peretti [1,2,3]★ Giovanni Morlino [4] Pasquale Blasi [2,3] and Pierre Cristofari [2,3,5]

[1]*Niels Bohr International Academy, Niels Bohr Institute, University of Copenhagen, Blegdamsvej 17, DK-2100 Copenhagen, Denmark*
[2]*Gran Sasso Science Institute, Viale F. Crispi 7, I-67100 L'Aquila, Italy*
[3]*INFN/Laboratori Nazionali del Gran Sasso, Via G. Acitelli 22, I-67100 Assergi (AQ), Italy*
[4]*INAF – Osservatorio Astrofisico di Arcetri, Largo Enrico Fermi 5, I-50125 Firenze, Italy*
[5]*Observatoire de Paris, PSL Research University, LUTH, 5 Place Jules Janssen, F-92195 Meudon, France*

Accepted 2022 January 8. Received 2022 January 8; in original form 2021 April 22

ABSTRACT

The enhanced star-forming activity, typical of starburst galaxies, powers strong galactic winds expanding on kiloparsec (kpc) scales and characterized by bubble structures. Here we discuss the possibility that particle acceleration may take place at the termination shock of such winds. We calculate the spectrum of accelerated particles and their maximum energy, which turns out to range up to a few hundred petaelectronvolt (PeV) for typical values of the parameters. Cosmic rays accelerated at the termination shock are advected towards the edge of the bubble excavated by the wind and eventually escape into extragalactic space. We also calculate the flux of gamma-rays and neutrinos produced by hadronic interactions in the bubble, as well as the diffuse flux resulting from the superposition of the contribution of starburst galaxies on cosmological scales. Finally, we compute the diffuse flux of cosmic rays from starburst bubbles and compare it with existing data.

Key words: acceleration of particles – neutrinos – cosmic rays – galaxies: starburst – gamma-rays: galaxies.

1 INTRODUCTION

Starburst galaxies (SBGs) are unique astrophysical objects characterized by an intense star formation rate (SFR), and a correspondingly higher rate of supernova (SN) explosions. Since SNe and winds of young stars are believed to be acceleration sites of cosmic rays (CRs), SBGs are likely to be powerful CR factories. The star-forming activity is often located in sub-kpc-sized regions, known as starburst nuclei (SBNs; Kennicutt 1998), with rather extreme conditions: high gas density ($n \gtrsim 10^2\,\mathrm{cm}^{-3}$), intense infrared–optical luminosity ($U_{\rm RAD} \gtrsim 10^3\,\mathrm{eV\,cm}^{-3}$), and strong magnetic fields ($B \gtrsim 10^2\,\mu\mathrm{G}$) are inferred in SBNs (Förster Schreiber et al. 2001; Mannucci et al. 2003; Gao & Solomon 2004; Thompson et al. 2006; Papadopoulos et al. 2011). The level of turbulence is also expected to be very high because of the repeated SN explosions and stellar winds. This turbulence is likely to slow down the spatial transport of charged high-energy (HE) particles, which therefore lose most of their energy inside SBNs. We refer to this mode of transport as *calorimetric*, and its implications have been discussed in detail by Yoast-Hull et al. (2013), Peretti et al. (2019), and Krumholz et al. (2020). Multiwavelength observational campaigns from radio to hard X-rays (see e.g. Carilli 1996; Williams & Bower 2010; Wik et al. 2014), and especially the spectra inferred from observations in the gamma-ray range, indicate that the transport of HE particles is strongly regulated by energy losses (see e.g. Ackermann et al. 2012; Peng et al. 2016; H. E. S. S. Collaboration et al. 2018; Ajello et al. 2020; Kornecki et al. 2020, 2022; Werhahn et al. 2021).

A peculiar aspect of SBGs is represented by the amount of target material for nuclear interactions, potentially leading to copious production of neutrinos and gamma-rays. The contribution of SBGs to the neutrino flux measured by the IceCube Observatory (IceCube Collaboration et al. 2013; Abbasi et al. 2021) has been extensively discussed by many authors (Loeb & Waxman 2006; Tamborra, Ando & Murase 2014; Bechtol et al. 2017; Sudoh, Totani & Kawanaka 2018; Palladino et al. 2019; Ajello et al. 2020; Peretti et al. 2020; Ambrosone et al. 2021a,b), together with the compatibility of the predictions with existing constraints imposed by gamma-ray observations (Ackermann et al. 2012; Lisanti et al. 2016). The seriousness of these constraints stimulated the search for powerful hidden CR accelerators in environments highly opaque to gamma-rays and yet transparent to neutrinos (Capanema, Esmaili & Serpico 2021) like the inner core of active galactic nuclei (AGNs; see e.g. Murase, Guetta & Ahlers 2016; Murase, Kimura & Mészáros 2020) or to reconsider the contribution from an extended region around the Galaxy (see e.g. Taylor, Gabici & Aharonian 2014; Blasi & Amato 2019; Recchia et al. 2021).

Recent anisotropy measurements performed by the Pierre Auger Observatory (Aab et al. 2018) support the idea that SBGs might play an important role in the production of ultrahigh-energy cosmic rays (UHECRs; see also Anchordoqui, Romero & Combi 1999; Anchordoqui 2018). This piece of information adds to previous indications of the existence of a CR component with light mass and possibly of extragalactic origin, in the energy region $\lesssim$EeV (Prosin et al. 2016; Arteaga-Velázquez et al. 2017; Aartsen et al. 2019).

Starburst winds have indeed been suggested to accelerate particles above PeV energies (Dorfi & Breitschwerdt 2012; Bustard, Zweibel & Cotter 2017) and subsequently produce photons through non-

★ E-mail: peretti@nbi.ku.dk

thermal processes (Romero, Müller & Roth 2018; Buckman, Linden & Thompson 2020; Müller, Romero & Roth 2020). These phenomena, together with the calorimetric transport of CRs and the intense photon backgrounds in SBNs, led to the careful investigation of the emission and absorption of gamma-rays in the central regions of SBGs, and the correlated neutrino emission (Peretti et al. 2019, 2020). Despite the potential importance of these astrophysical objects for a variety of phenomena, the modelling of the processes of acceleration and interaction of CRs in SBGs remains rather poor and yet it is crucial if to assess their role as sources of high energy radiation and CRs in a reliable way.

As stated above, particles are not only accelerated in the nuclei of SBGs, but also in the (kpc-sized) wind structures expanding from the SBN region to the circumgalactic medium (CGM). While in our previous works on SBGs (Peretti et al. 2019, 2020), we focused our attention on phenomena occurring inside the SBN, here we discuss the starburst winds as potential additional sites for particle acceleration and interactions.

Starburst winds are inferred to be powered by the mechanical energy and heat produced by SNe and young stars possibly combined with some contribution due to the radiation pressure (see e.g. Zhang 2018). The intense activity heats and pressurizes the interstellar medium (ISM; see Westmoquette et al. 2009a,b, for detailed observation of M82) creating a hot cavity and eventually inflating a powerful thermally driven wind bubble (see Veilleux, Cecil & Bland-Hawthorn 2005). Starburst winds are characterized by high mass-loss rate ranging from a few $M_\odot\,yr^{-1}$ for moderate starbursts up to $10^2\,M_\odot\,yr^{-1}$ in ultraluminous infrared galaxies (ULIRGs; see Cicone et al. 2014, for details) or starburst coexisting with (or replaced by) AGNs (see e.g. Lamastra et al. 2016, 2019; Wang & Loeb 2017; Liu et al. 2018).

Measurements of the wind speed are often based on detection of spectral lines associated with the warm and cold phases of the ISM embedded in the wind bubble and indicate velocities of the order of hundreds of $km\,s^{-1}$. On the other hand, theoretical models and X-ray observations show that the hot phase of the wind has a much higher velocity of the order of $10^3\,km\,s^{-1}$ (see e.g. Strickland & Heckman 2009). These fast outflows easily break out of their galactic discs and expand into the surrounding galactic haloes (see Chevalier & Clegg 1985, hereafter CC85).

Wind bubbles are characterized by an innermost region of fast and cool wind powered by a central engine. The fast wind region extends up to the wind termination shock (also referred to as the wind shock), where the wind plasma is slowed down and heated up. A forward shock expands into the CGM, typically with transonic velocity. Between the two shocks the contact discontinuity separates the shocked wind from the shocked swept-up halo medium (see e.g. Koo & McKee 1992a). The starburst activity can last for hundreds of millions of years (Myr) thus potentially producing an approximately steady injection of particles during this time (see Di Matteo et al. 2008; McQuinn et al. 2009; Bustard et al. 2017).

Here we investigate the process of diffusive shock acceleration (DSA) of particles at the wind termination shock of starburst-driven winds, and estimate the associated production of gamma-rays and neutrinos produced in the entire bubble excavated by the wind, and the flux of protons escaping such bubble. We adopt the semi-analytic approach to CR transport at the termination shock, as developed by Morlino et al. (2021, hereafter MBPC21) for the case of winds associated with star clusters. This theoretical approach allows us to establish a direct connection between the environmental conditions in the wind and the particle acceleration process, with special attention for the maximum energy of accelerated particles. Moreover the transport of the non-thermal particles in the entire wind bubble is described rigorously, taking into account diffusion, advection, adiabatic losses and gains, as well as catastrophic energy losses. This enables us to calculate the cumulative contribution of starburst winds to the diffuse gamma-ray and neutrino fluxes exploring the associated proton flux that we could observe at Earth as CRs above the *knee*.

Our investigation shows that (1) protons can be accelerated up to hundreds of PeV at the starburst wind termination shock; (2) gamma-rays and neutrinos are produced as secondary products of pp and pγ interactions in these systems, possibly leading to detectable spectral features; (3) the contribution of starbursts to the diffuse neutrino flux can be dominant without exceeding the diffuse gamma-ray flux observed by *Fermi*-Large Area Telescope (LAT); and (4) accelerated particles escaping starburst systems can provide a sizeable contribution to the light CR component observed above the knee.

The structure of this paper is as follows. In Section 2, we provide a description of the wind bubble. In Section 3, we describe the modelling of acceleration and transport in the system, and provide the main details of our semi-analytical approach to CR transport. In Section 4, we discuss the solution of the transport equation and the corresponding maximum energy as a function of the relevant parameters. We also show the associated gamma-ray and neutrino fluxes and the flux of CR protons escaping the bubble, for some benchmark cases. In Section 5, we explore the multimessenger potential of the combined contribution of wind bubbles in the context of the diffuse fluxes observed at Earth. In Section 6, we summarize our results and draw our conclusions.

2 EVOLUTION AND PROPERTIES OF THE WIND BUBBLE

The typical lifetime of a starburst event is of order ∼200–300 Myr (Di Matteo et al. 2008): at formation the structure is fuelled by energy and mass released by young OB and Wolf–Rayet stars for about 6 Myr. After this initial stage, the first core-collapse SN explosions are expected to take place. The energy and mass that they release dominates over the ones due to the young stars activity. In the minimal assumption of an *instantaneous* starburst trigger, the activity would run out in about 40 Myr when $8\,M_\odot$ stars end their life (see also Veilleux et al. 2005). In practice, the actual duration of a starburst is determined by the star-forming activity, which can last up to few hundred million years, as mentioned earlier. Such time-scale is much longer than the typical duration of the processes of particle acceleration and transport in the bubble produced by the starburst activity, so that from this point of view, SBGs and their wind superbubbles can be considered as steady-state systems for HE particles (see also Zirakashvili & V"olk 2006; Bustard et al. 2017, for related discussions).

The engine of a starburst-driven galactic wind is the activity of SNe and massive stars that heat and pressurize the ISM excavating a hot bubble where temperature and pressure are $T \sim 10^8\,K$ and $P/k_B \sim 10^7\,K\,cm^{-3}$ (as also discussed in CC85). Once the starburst event has started, the bubble expands above and below the galactic disc due to the pressure unbalance between its interior and the unshocked host galaxy ISM and eventually reaches the scale height of the disc, breaking out into the galactic halo. Inside the disc, instead, the bubble remains confined by the ISM pressure (see Tenorio-Tagle & Muñoz-Tuñón 1997; Cooper et al. 2007). As shown in recent numerical simulations (Fielding, Quataert & Martizzi 2018; Schneider et al. 2020), the clustered activity of SNe typical of SBNs is

strong enough to drive and sustain a powerful galactic outflow. In this framework, CRs could also contribute as a supplementary ingredient powering an outflow in very active star-forming galaxies as discussed by Hanasz et al. (2013). However, their importance in contributing to the wind launching is highly uncertain due to the possible impact of the dense and turbulent environment on their transport (see e.g. Krumholz et al. 2020) and their severe energy losses in the core of SBGs (see e.g. Peretti et al. 2019; Werhahn et al. 2021; Kornecki et al. 2022). On the other hand, in the case of a less intense and spatially extended star formation, typical of the spiral arms of mild star-forming galaxies, where energy losses are usually negligible, the additional contribution of CRs (see e.g. Breitschwerdt, McKenzie & Voelk 1991; Everett et al. 2008; Recchia, Blasi & Morlino 2016; Pfrommer et al. 2017; Girichidis et al. 2022) and radiation pressure may be necessary to launch a galactic outflow (see e.g. Zhang 2018).

The dynamics of starburst winds (Strickland & Stevens 2000; Strickland et al. 2002) is qualitatively similar to that of stellar winds and winds of star clusters (Castor, McCray & Weaver 1975; Weaver et al. 1977; Koo & McKee 1992a,b) when the galactic ISM is roughly homogeneous (Strickland et al. 2002). However, when the medium is inhomogeneous, as expected in realistic cases (Westmoquette et al. 2009a,b), the hot gas follows the path of least resistance out of the disc, resulting into a non-homogeneous outflow. Once in the halo, the hot gas expands freely and the geometry can be reasonably assumed to be spherical (see Cooper et al. 2007). For our purposes, the assumption of a spherical geometry is well motivated by the fact that accelerated particles probe large distances, averaging out any spatial inhomogeneities.

Radiative losses can affect the wind dynamics and several theoretical and numerical works investigated the possible role of such losses, leading to a wide range of possible scenarios (see Bustard, Zweibel & D'Onghia 2016; Zhang 2018, and references therein). If the starburst wind is approximately adiabatic (as shown in numerical simulations; see e.g. Fielding et al. 2017; Schneider et al. 2020), its behaviour is in good agreement with the analytic model developed in CC85, and adopted in this work.

The first stage of the evolution of the wind bubble is characterized by a free expansion that ends when the mass of the swept-up ambient medium becomes comparable to the mass injected in the form of a wind ($t_{\rm free} \lesssim 1$ Myr for an average halo density $n_{\rm h} \approx 10^{-3}$ cm^{-3}). The wind is supersonic, so that it is preceded by a forward shock, while a reverse shock is launched towards the interior, the so-called termination shock. During the free expansion phase, the two shocks move outwards but staying very close to each other. The shocked wind and the shocked ISM are separated by a contact discontinuity. When the accumulated mass eventually becomes larger than the mass added in the form of a wind, the outflow decelerates appreciably. If the CGM is assumed to be spatially homogeneous, the radius of the forward shock changes in time as $R_{\rm FS} \propto t^{3/5}$, while the termination shock follows the trend $R_{\rm sh} \propto t^{2/5}$ (see Weaver et al. 1977; Koo & McKee 1992a). The bubble eventually reaches a pressure-confined state, typically after a few tens of Myr. This late stage of the evolution is characterized by a pressure balance between the cool wind ram pressure and the pressure of the undisturbed halo medium $P_{\rm h}$ (which, in turn, is in equilibrium with the pressure of the shocked wind). At this point, the wind shock is stalled while the contact discontinuity and the forward shock keep slowly expanding in the CGM. As detailed in Lochhaas et al. (2018) (see also Strickland & Stevens 2000), the dynamics of the wind bubble depends on the density profile of the CGM gas.

The structure of the starburst-driven wind bubble can be pictured as onion like (see top panel of Fig. 1). The SBN, responsible for launching and powering the outflow, is located at the centre of the system. The wind speed increases approaching the boundary of the SBN, where it becomes supersonic and quickly reaches its terminal velocity (V_∞). At this point the wind velocity remains basically constant (see CC85 and lower panel of Fig. 1), up to the termination shock (located at $R_{\rm sh}$), where the wind is slowed down and heated up. As we discuss below, this configuration is very interesting from the point of view of particle acceleration, in that the upstream region is in the direction of the SBN, hence particle escape from the upstream region is inhibited and becomes possible only through the external boundary of the wind bubble. The medium in which a galactic wind bubble expands affects the spatial structure of the bubble. Galactic haloes are inferred to be characterized by a hot diffuse gas component where typically $n_{\rm h} \lesssim 10^{-2}$ cm^{-3} and $T_{\rm h} \sim 10^6$–10^7 K (Anderson, Churazov & Bregman 2016; Tumlinson, Peeples & Werk 2017). Hence, in a starburst CGM the thermal pressure is expected to be $P_{\rm h}/k_{\rm B} \lesssim 10^5$ K cm^{-3} (where $k_{\rm B}$ is the Boltzmann constant).

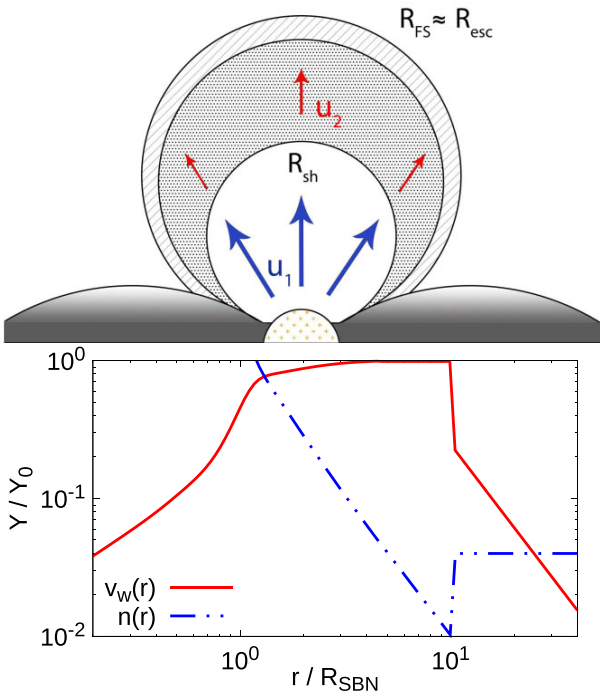

Figure 1. Top panel: structure of the wind bubble. The SBN, from which the wind is launched, is located in the centre of the galactic disc. The blue (red) arrow corresponds to the cool (shocked) wind region. The wind shock ($R_{\rm sh}$) separates the two regions. The forward shock (at $R_{\rm FS}$) bounds the system from the undisturbed halo region (credit: I. Peretti). Bottom panel: wind profile (thick red) and particle density profile (dot–dot–dashed blue), where Y is the density or velocity, and Y_0 is the normalizing density or velocity. The plot is in arbitrary units for illustrative purposes. The location of the wind shock is assumed to be at 10 $R_{\rm SBN}$ for illustrative purposes.

In evolved wind bubbles, the balance between the thermal pressure in the halo and the wind ram pressure, $\rho\, v_{\rm w}^2$, sets the position of the termination shock:

$$R_{\rm sh} \approx \sqrt{\frac{\dot{M} V_\infty}{4\pi\, P_{\rm h}}} = 6.2\, \dot{M}_0^{1/2}\, V_{\infty,8}^{1/2}\, P_{\rm h,4}^{-1/2}\, {\rm kpc}, \quad (1)$$

where $\dot{M}$ ($\dot{M}_0$) is the wind mass-loss rate (in units of 1 M$_\odot$ yr^{-1}), $V_{\infty,8}$ is the terminal wind speed in units of 10^8 cm s^{-1}, and $P_{\rm h,4}$ is

the halo pressure in units of $10^4\,k_{\rm B}\,{\rm cm}^{-3}\,{\rm K}$. These three parameters characterize the global properties of the system (see also Veilleux et al. 2005; Strickland & Heckman 2009, for additional details and connection to the core activity). While the termination shock is approximately stalled, the forward shock continues to expand as

$$R_{\rm FS} \approx 10\left[\dot{E}_{43} n_{\rm h,-3}^{-1}\right]^{1/5} t_7^{3/5}\,{\rm kpc}, \tag{2}$$

where $\dot{E}_{43} = [\dot{M}\,V_\infty^2/2]/10^{43}\,{\rm erg\,s^{-1}}$ is the wind power, $n_{\rm h,-3}$ is the halo density in units of $10^{-3}\,{\rm cm}^{-3}$, and t_7 is the time in units of 10 Myr (see also Koo & McKee 1992a). It follows that the typical Mach number of the forward shock is of order unity, starting at times of order ∼10 Myr. This is the main reason why efficient particle acceleration is not expected to take place at the forward shock.

At the termination shock the conditions are more favourable. The temperature of the plasma at the wind shock sets the local sound speed. The adiabatic expansion cools the gas as $T \propto r^{-4/3}$, so that assuming a SBN size $R_{\rm SBN} \sim 200\,{\rm pc}$ and $R_{\rm sh}$ as given by equation (1), one can expect a temperature $T \approx 10^6\,{\rm K}$ at the wind shock when the SBN is as hot as $T_{\rm SBN} \approx 10^8\,{\rm K}$. Therefore, the sound speed of the free expanding wind at the shock is $c_{\rm s} \approx 10^2\,T_6^{1/2}\,{\rm km\,s^{-1}}$. As a consequence the Mach number of the plasma at the wind shock is of order ∼10 making it the only plausible site for particle acceleration in the wind-bubble system.

For the innermost regions of the system (the SBN and the cool wind) we adopt a smooth parametrization of the model of CC85 for the velocity profile (see bottom panel Fig. 1). The model describes a wind where the velocity increases toward the edge of the SBN. At the SBN boundary the wind becomes supersonic and quickly reaches V_∞, while beyond the termination shock, the gas gets heated and slowed down. At the termination shock we adopt the jump condition appropriate for a strong shock so that $u_1 = V_\infty$ and $u_2 = u_1/4$. Moreover, for adiabatic expansion, the shocked wind moves with a velocity that drops with distance as $\sim r^{-2}$, namely $ur^2 = $ constant. The wind plasma is assumed to be fully ionized, while the density in the SBN is assumed to be dominated by dense molecular gas. Hence the particle density in the system (blue dot–dot–dashed curve in Fig. 1) can be approximated as

$$\rho(r) = \begin{cases} \rho_{\rm SBN} & r < R_{\rm SBN}, \\ \frac{\dot{M}}{4\pi r^2 v_{\rm w}(r)} & R_{\rm SBN} < r < R_{\rm sh}, \\ 4 \times \frac{\dot{M}}{4\pi R_{\rm sh}^2 u_1} & R_{\rm sh} < r < R_{\rm FS}. \end{cases} \tag{3}$$

For the purpose of estimating the diffusion coefficient for HE particles in the bubble, we assume that a fraction $\epsilon_{\rm B}$ (in MBPC21 we have used $\eta_{\rm B} = \epsilon_{\rm B}/2$) of the kinetic energy density of the free expanding wind is converted at any given radius into turbulent magnetic field energy density. We also assume that at the termination shock the perpendicular components of the magnetic field are compressed by a factor of 4, which implies that the strength of the magnetic field downstream is enhanced by a factor of $\sqrt{11}$ and remains spatially constant in the downstream region.

Overall, the strength of the magnetic field can be written as

$$B(r) = \begin{cases} \frac{\sqrt{\epsilon_{\rm B}\dot{M} v_{\rm w}(r)}}{r} & r < R_{\rm sh}, \\ \sqrt{11} \times \frac{\sqrt{\epsilon_{\rm B}\dot{M} u_1}}{R_{\rm sh}} & r > R_{\rm sh}, \end{cases} \tag{4}$$

where the radial dependence of the upstream wind profile, $v_{\rm w}(r)$, has a negligible impact on the magnetic field in the corresponding region.

Assuming that the turbulent field gets organized according to a power spectrum $P(k) \propto k^{-\delta}$, the corresponding diffusion coefficient due to resonant particle scattering can be estimated as

$$D(r,\,p) = \frac{1}{3} r_{\rm L}(r,\,p)\,v(p)\left[\frac{L_{\rm c}}{r_{\rm L}(r,\,p)}\right]^{\delta-1}, \tag{5}$$

where $r_{\rm L}$ is the Larmor radius, v the particle velocity, and $\delta = 5/3$ (3/2) for Kolmogorov (Kraichnan) turbulence. Bohm diffusion would correspond to $\delta = 1$. The quantity $L_{\rm c}$ denotes the energy containing scale of the turbulence. For momenta $p > p^*$, where p^* is defined such that $r_{\rm L}(p^*) = L_{\rm c}$, the diffusion coefficient changes its energy dependence due to lesser power on larger scales and can be written as (Subedi et al. 2017; Dundovic et al. 2020)

$$D(r,\,p) = \frac{1}{3} L_{\rm c}\,v(p)\left[\frac{r_{\rm L}}{L_{\rm c}}\right]^2 \quad p > p^*. \tag{6}$$

In this work, we adopt a Kraichnan spectrum of the turbulence, $\delta = 3/2$ as the reference scenario, and we assume $L_{\rm c}$ to be comparable with the size of the SBN, namely $L_{\rm c} \sim 10^2\,{\rm pc}$.

3 MODEL

In this section, we provide a detailed description of the theoretical model. In Section 3.1, we present the solution of the CR transport equation of particles accelerated at the wind shock of the starburst-driven wind bubble. Together with the solution we additionally describe the flux of escaping particles. In Section 3.2, we describe the calculation of gamma-rays and neutrinos from pp and pγ interactions.

3.1 Particle acceleration at the termination shock

Particle acceleration is assumed to take place at the termination shock. For the sake of simplicity we adopt a spherical symmetry neglecting the deformation induced by the surrounding medium. The bubble is assumed to be already evolved through the deceleration phase, so that the shock location is given by equation (1).

The transport of non-thermal particles in the bubble is determined by diffusion, adiabatic energy losses and gains, advection with the wind, and catastrophic energy losses, which are dominated by pp inelastic collisions in the SBN, for those particles that have high enough energy to diffuse against the wind and reach the central region. The transport equation that we solve can be written as follows:

$$\frac{\partial}{\partial r}\left[r^2 D(r,\,p)\frac{\partial f}{\partial r}\right] - r^2 v_{\rm w}(r)\frac{\partial f}{\partial r} + \frac{{\rm d}\left[r^2 v_{\rm w}(r)\right]}{{\rm d}r}\frac{p}{3}\frac{\partial f}{\partial p} + r^2 Q(r,\,p) - r^2\Lambda(r,\,p) f = 0, \tag{7}$$

where $f = f(r,\,p)$ is the particle distribution function, $D(r,\,p)$ is the diffusion coefficient (in general space dependent), $v_{\rm w}(r)$ is the wind profile, $Q(r,\,p)$ is the injection term, and $\Lambda(r,\,p)$ is the rate of energy losses.

Assuming that particle injection only takes place at the location of the termination shock and is limited to a single momentum $p_{\rm inj}$, we can write

$$Q(r,\,p) = \frac{Q_0(p)}{4\pi r^2}\,\delta[r - R_{\rm sh}] = \frac{\eta_{\rm inj} n_1 u_1}{4\pi p^2}\,\delta[p - p_{\rm inj}]\,\delta[r - R_{\rm sh}], \tag{8}$$

where n_1 and u_1 are the density and wind speed immediately upstream of the shock, and $\eta_{\rm inj}$ is the fraction of particles involved in the acceleration process. We take $\eta_{\rm inj}$ such that the pressure of accelerated particles is limited to a fraction ∼10 per cent of the wind ram pressure at the shock. Notice that, as long as the shock compression factor is larger than 2.5 (meaning that the spectrum is harder than p^{-5}),

the value of $p_{\rm inj}$ does not play any relevant role in the normalization of equation (8). The loss term takes into account energy losses for proton–proton collisions:

$$\Lambda(r,\,p) = n(r)\sigma_{\rm pp}(p)v(p)\,, \tag{9}$$

where v is the particle speed, $n(r) = \rho(r)/m_{\rm p}$ is the target density in the wind, and $\sigma_{\rm pp}$ is the cross-section (Kelner, Aharonian & Bugayov 2006). We neglect losses due to pγ interactions since, as we show below, the maximum energy that particles reach is barely enough to exceed the kinematic threshold for this process, using optical (OPT) and ultraviolet (UV) photons as targets.

Equation (7) is solved by following the technical procedure put forward in MBPC21 for the case of winds from star clusters. We refer the reader to that paper for details, while here we only summarize the main equations that allow us to obtain the solution of the problem by iterations. We also discuss the differences with respect to MBPC21, mainly due to the presence of energy losses.

The method starts from determining the solution of the transport equation upstream and downstream separately and then imposes the continuity of the solution at the shock location. The solution in the upstream region reads

$$f_1(r,\,p) = f_{\rm sh}(p)\,{\rm e}^{-\int_r^{R_{\rm sh}} {\rm d}r'\,V_1(r',p)/D_1(r',p)}, \tag{10}$$

where $f_{\rm sh}$ is the particle distribution function at the shock and V_1 is an effective velocity *felt* by particles upstream, due to the combination of spherical symmetry and energy losses:

$$V_1(r,\,p) = u_1(r) + \frac{G_1(r,\,p) + H_1(r,\,p)}{r^2\,f_1(r,\,p)}. \tag{11}$$

The functions G_1 and H_1 describe adiabatic energy losses and gains and catastrophic energy losses, respectively, and are reported in Appendix B

In the downstream region, the solution is made easier by the fact that the flow is divergence free (namely ur^2 is constant) and energy losses due to pp scatterings are negligible. This simplification allows us to write

$$f_2(r,\,p) = f_{\rm sh}(p)\frac{1-{\rm e}^{\alpha(r,p)-\alpha(R_{\rm esc},p)}}{1-{\rm e}^{-\alpha(R_{\rm esc},p)}}, \tag{12}$$

where

$$\alpha(r,\,p) = \frac{R_{\rm sh}\,u_2}{D_2(p)}\left(1-\frac{R_{\rm sh}}{r}\right) \tag{13}$$

and $R_{\rm esc} \approx R_{\rm FS}$ is the location where particles escape from the system and assumed to be equal to the forward shock radius. Integrating the transport equation in a narrow region around the termination shock we find an equation for $f_{\rm sh}(p)$, after using the solution upstream and downstream to evaluate the spatial derivatives on the two sides of the shock:

$$f_{\rm sh}(p) = \frac{s\,n_1\,\eta_{\rm CR}}{4\pi\,p_{\rm inj}^3}\left(\frac{p_{\rm inj}}{p}\right)^s {\rm e}^{-[\Gamma_1(p)+\Gamma_2(p)]}. \tag{14}$$

Here Γ_1 and Γ_2 describe the departure from the standard solution p^{-s} that would have been obtained at a plane infinite shock, due to a variety of factors:

$$\Gamma_1(p) = s\int_{p_{\rm inj},}^{p}\frac{{\rm d}p'}{p'}\frac{G_1(R_{\rm sh},\,p')+H_1(R_{\rm sh},\,p')}{u_1 R_{\rm s}^2 f_{\rm sh}(p')}, \tag{15}$$

$$\Gamma_2(p) = s\int_{p_{\rm inj},}^{p}\frac{{\rm d}p'}{p'}\frac{u_2/u_1}{{\rm e}^{\alpha(p',R_{\rm esc})}-1}. \tag{16}$$

The function Γ_1 reflects the effects of spherical symmetry and losses upstream, and is appreciably different from unity at energies close to the maximum energy, namely at energies where D_1/u_1 becomes comparable to $R_{\rm sh}$ (see also Berezhko & Völk 1997). For the particles that are energetic enough to reach the SBN, energy losses in the dense gas become important both for CR transport (if $\dot{M}$ is large enough) and production of secondary radiation (see Bustard et al. 2017; Merten et al. 2018, for related discussions). However, in all cases that we have studied this phenomenon never leads to observable consequences.

Notice that equation (14) expresses the solution in a recursive form, because both G_1 and H_1 are function of f. The actual solution is obtained using an iterative technique as described in MBPC21.

The spectral modification due to the transport in the downstream region is contained in the function Γ_2, which becomes important when the diffusion length of particles ($\lambda_{\rm D} \sim D_2/u_2$) becomes comparable to the size of the shocked-wind region ($R_{\rm esc} - R_{\rm sh}$).

The escape flux at the bubble boundary, defined as $j_{\rm esc} = -D\,\partial_r f(R_{\rm esc})$, can be easily derived from equation (12):

$$j_{\rm esc}(p) = u_2\,f_{\rm sh}(p)\frac{[R_{\rm sh}/R_{\rm esc}]^2}{1-{\rm e}^{-\alpha(R_{\rm esc},p)}}, \tag{17}$$

and the total flux of escaping particles is $J_{\rm esc} = 4\pi R_{\rm esc}^2\,j_{\rm esc}$.

The escape flux modifies the solution at the shock only very mildly and only for very high particle energies. On the other hand the spatial extent of the downstream region (shocked wind), which in turn depends on the age of the bubble, reflects rather strongly on the gamma-ray and neutrino signal from a SBG.

The assumption of stationarity adopted in the equation requires that the acceleration process is much faster than the time for dynamical evolution of the system. This is typically the case, but as a consistency check, we always verify that the acceleration time defined as

$$t_{\rm acc}(p) = \frac{3}{u_1-u_2}\int_0^p\frac{{\rm d}p'}{p'}\left[\frac{D_1(p')}{u_1}+\frac{D_2(p')}{u_2}\right] \tag{18}$$

be shorter than the lifetime of the system (see e.g. Blasi 2013).

3.2 Production of secondaries

As discussed in Section 3.1 (see also Appendix A for additional details), pp and pγ interactions in the downstream region take place with typical time-scales larger than Gyr, so that their dynamical impact on the CR transport can be neglected. However, the luminosity of the wind bubble can be a sizable fraction of the SBN's luminosity due to the large spatial extent of the system (see also Romero et al. 2018; Müller et al. 2020, for related discussions).

We thus compute the gamma-ray and neutrino emission resulting from the interaction of CRs with (i) particles in the plasma through pp interactions and (ii) thermal photons, as produced by stars and dust in the galaxy and illuminating the wind bubble itself (pγ interactions).

The calculation of gamma-rays produced through pp interactions has been performed using the NAIMApackage (Kafexhiu et al. 2014), which implements the procedure described in Kelner et al. (2006), while the gamma-rays produced through pγ interactions are computed following Kelner & Aharonian (2008). The gamma-ray absorption inside the SBN is taken into account as in Peretti et al. (2019), where the background photon field is assumed to be constant in the SBN volume. On the other hand, the size of the system and the r^{-2} dependence of the photon field imply negligible absorption effects for gamma-rays produced in the wind bubble. Finally, the gamma-ray absorption on the extragalactic background light (EBL) on cosmological distances is computed adopting the EBL model of Franceschini & Rodighiero (2017).

Table 1. Parameters for the benchmark cases B0 and B1. The resulting maximum energy and monochromatic single flavour neutrino flux at 25 TeV are reported at the bottom. The latter is computed assuming a fiducial luminosity distance $d_L = 3.9$ Mpc.

	B0	B1
$\dot{M}$ ($M_\odot$ yr^{-1})	5	10
V_∞ (10^3 km s^{-1})	2	3
P_h/k_B (10^4 K cm^{-3})	2.5	8
t^*_{age} (Myr)	250	250
R_{sh} (kpc)	12.36	11.97
R_{FS}/R_{sh}	4	4.6
E_{max} (PeV)	44	131
$\tilde{F}_{\nu_\mu}$ $\left(10^{-11}\ \frac{GeV}{cm^2\ s}\right)$	1.27	8.9

The single flavour neutrino flux is computed assuming equipartition among flavours, $(\nu_e, \nu_\mu, \nu_\tau) = (1{:}1{:}1)$, due to flavour oscillations during propagation to the Earth. The production of neutrinos in pp interactions is estimated by rescaling the gamma-ray luminosity as $L_\nu(E_\nu) \approx L_\gamma(E_\gamma)/2$, where $E_\gamma \approx 2E_\nu$. The neutrinos produced in the $p\gamma$ interactions are computed following Kelner & Aharonian (2008).

4 EMISSION FROM INDIVIDUAL STARBURSTS

In this section, we discuss the results of the calculation of the spectra of accelerated particles and HE gamma-rays and neutrinos (Section 4.1) for an individual SBG and how the properties of the bubble and of the accelerated particles change when changing parameters (Section 4.2).

4.1 Particles and spectra

We discuss two stereotypical models of SBGs so as to illustrate how the results change by changing the properties of the SBN. The two benchmark cases are labelled as B0 and B1 and correspond to the parameters' values reported in Table 1. The B0 prototype is reminiscent of local mild SBGs such as M82 and NGC 253. We assume the photon field of NGC 253 (Galliano, Dwek & Chanial 2008) as representative of the prototype B0. Observations and numerical simulations of M82 suggest a terminal (wind) velocity $\sim$2000 km s^{-1} (Strickland & Heckman 2009; Melioli, de Gouveia Dal Pino & Geraissate 2013), with a mass-loss rate up to $\lesssim 3\ M_\odot$ yr^{-1}. Similar terminal wind speed but higher mass-loss rate is inferred for NGC 253 (Strickland et al. 2002; Bolatto et al. 2013). The B1 configuration represents a somewhat more powerful wind that can be expected in objects for which the nuclear activity and temperature is higher [such as luminous infrared galaxies (LIRGs)] than what is inferred for M82 and NGC 253 (see e.g. Bustard et al. 2017). For the B1 prototype we assume that the photon background is somewhat larger than B0 and for reference we assume the spectral energy distribution (SED) of NGC 1068 (Galliano et al. 2008).

In Table 1, we also show the maximum energy of accelerated particles, E_{max}, and the single flavour neutrino energy flux produced in the wind bubble at 25 TeV, defined as $\tilde{F}_{\nu_\mu}$, as observed from a distance of 3.9 Mpc. Both these quantities are outputs of our calculations. The positions of the termination shock, equation (1), and of the edge of the bubble, equation (2), for the two prototypes are calculated fixing the age of the system to $t^*_{age} = 250$ Myr and by assuming a value of the pressure in the external medium, P_h/k_B.

Results for the cases B0 and B1 are reported in Figs 2 and 3, respectively. The top panels show the particle spectrum at the shock,

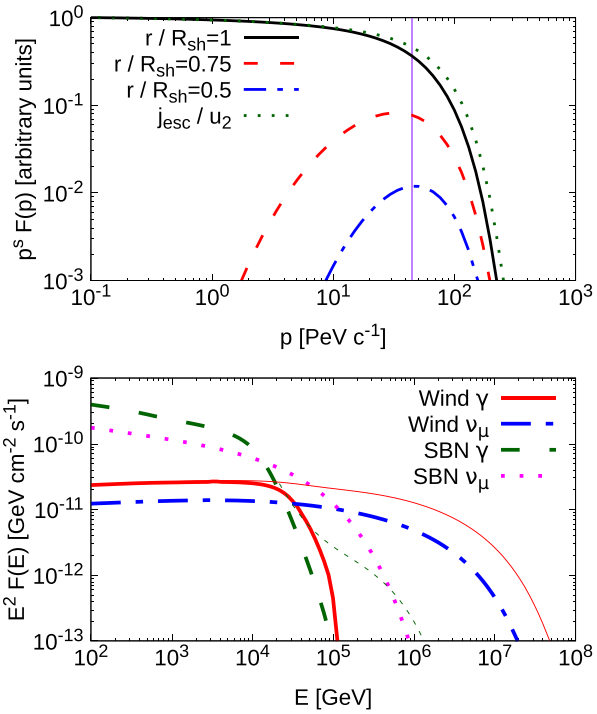

Figure 2. Particle spectrum and high-energy (HE) multimessenger spectra at Earth assuming $d_L = 3.9$ Mpc for the benchmark prototype B0. Top panel: proton spectrum at the shock (thick black line) compared to the solution at $0.75R_{sh}$ (red dashed line) and $0.5R_{sh}$ (blue dot–dashed line). The escape flux is also shown (green dotted line). Bottom panel: gamma-ray and neutrino flux from the wind (thick red and dot–dashed blue lines) compared to the emission from the SBN core (green dashed and pink dotted lines). The effect of EBL absorption is taken into account assuming a distance of 3.9 Mpc. For comparison, and for a qualitative view of the $\gamma\gamma$ absorption in the source, the gamma-ray components are shown when the EBL absorption is neglected (thin lines).

the escaping flux, and the particle spectrum in the cold-wind region as computed at different radii ($0.75R_{sh}$ and $0.50R_{sh}$). The vertical purple line identifies the position of the maximum momentum p_{max} of accelerated particles, defined as the value at which the spectrum $p^s f(p)$ is reduced by e. The bottom panels of the same figure show the corresponding spectra of gamma-rays and neutrinos resulting from pp and pγ interactions computed for the cases of a strong shock ($s = 4$) and assuming that the source is located at a distance of $\sim$3.9 Mpc (appropriate for M82). The red thick (thin) solid line shows the gamma-ray emission from the wind region after (before) correcting for absorption on the EBL during transport from the source to Earth. Notice that the same plots report also the contribution of gamma-rays and neutrinos produced by the interaction of CRs accelerated by supernova remnants (SNRs) inside the SBN and interacting inside the nucleus, assuming a source spectrum $\sim p^{-4.2}$, as inferred for M82 by Peretti et al. (2019), with a maximum energy $\lesssim$1 PeV. The thick (thin) line refers to the flux after (before) correction for absorption en route.

The flux of muon neutrinos from the wind region is shown as a blue thick dash–dotted line. Such flux is dominated by the contribution of pion production in pp interactions downstream of the termination shock. In Fig. 3, due to the larger luminosity of the SBG, the contribution to the neutrino flux due to photomeson production

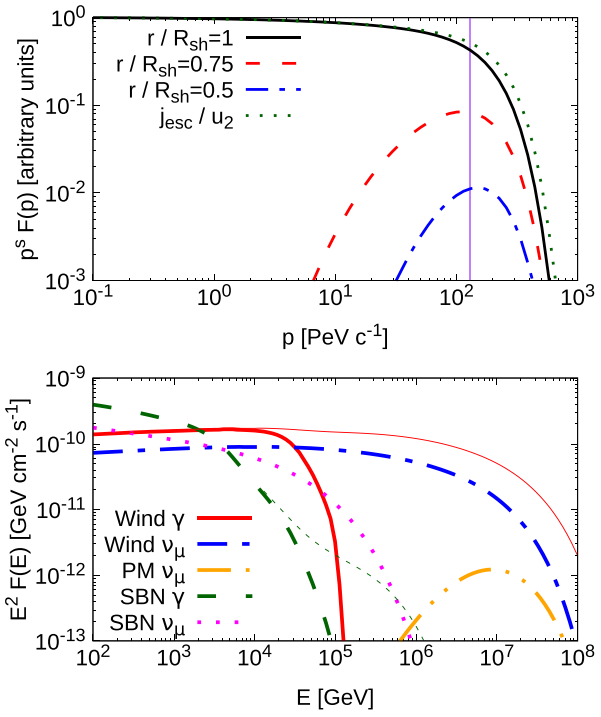

Figure 3. Particle and high-energy (HE) multimessenger spectra for the benchmark prototype B1. The line style and colours are identical to Fig. 2. The only difference is that the production of photomeson neutrinos from the wind bubble (orange dot–dot–dashed curve) becomes relevant at ∼10 PeV.

(dash–dot–dotted orange line) becomes visible in the plot. Such flux is present only in the highest energy region because of the kinematic threshold of the process of photopion production.

A few comments on the spectrum of accelerated particles (top panels in Figs 2 and 3) are in order: as it would be the case for standard DSA, the spectrum of accelerated particles is a power law when the momentum is much smaller than the maximum one. On the other hand, as discussed in MBPC21, spherical symmetry induces a dependence of the spectrum on the diffusion coefficient that is most marked around $p_{\rm max}$. This is because particles can *feel* an effective plasma velocity that is smaller than $v_{\rm w}$ when their diffusion length becomes comparable with $R_{\rm sh}$. Particles with high energies can travel farther away from the shock and feel its curvature in a more prominent way. The deviation from the standard power law is more visible for weak energy dependence of the diffusion coefficient. In other words, the deviation from a power law would start at lower energies for Kolmogorov diffusion, while it would occur closer to $p_{\rm max}$ for Bohm diffusion (see discussion in MBPC21). These subtle effects also reflect in the spectrum of secondary gamma-rays and neutrinos. The maximum energy reached by accelerated particles varies between tens of PeV for the prototype B0 to $\gtrsim$100 PeV for B1.

As previously mentioned, here we assumed $s = 4$, but in Section 6 we discuss the case of softer slopes as might arise due to the motion of scattering centres in the downstream plasma (see Caprioli, Haggerty & Blasi 2020, for details).

By looking at the particle spectrum in the inner region, one can conclude that only particles at the maximum energy can diffuse efficiently against the wind and populate the inner region of the system. Nevertheless, it appears clear that, unless an additional acceleration mechanism is present in the system, the number of particles that can successfully diffuse back to the SBN is strongly suppressed due to the geometry of the system. Indeed, in order to successfully diffuse upwind towards the SBN, particles need to have a momentum $p_{\rm b}$ such that the diffusion length becomes larger than the upstream region, namely $D(p_{\rm b})/u_1 \gtrsim R_{\rm sh}$. Finally, we notice that the spectrum of the escaping flux, as also discussed in MBPC21, does not differ strongly from the solution at the shock in terms of spectral slope and maximum energy.

The gamma-ray emission from the SBG is dominated by the emission of the SBN for $E \lesssim$ TeV. However, depending on the total power of the system and the conditions of the external medium where the bubble is expanding into, the emission from the wind region may become dominant at high enough energy and be identifiable as an extension of the spectrum up to the energy for which there is a substantial absorption on the EBL. In the scenario where accelerators in the SBN cannot exceed ∼PeV, all neutrinos with energy $\gtrsim 10^2$ TeV are produced in the wind and the luminosity increases with $\dot{M}$ since this parameter directly affects the target density for pp interactions (see also Table 1). The slope of the neutrino spectra below ∼10 TeV is slightly harder than E^{-2} due to the energy dependence of the cross-section for pp inelastic collisions, $\sigma_{\rm pp}$. Above ∼10 TeV the spectral slope gets gradually softer due to the shape of the parent proton population. The hadronic emission from the wind is dominated by the pp interaction taking place in the shocked-wind region, whereas the contribution from the free-wind region might be relevant only for extreme values of $\dot{M}$, or possibly during some early stages of the bubble evolution. The photomeson contribution is found to be always subdominant compared to the pp and is irrelevant if $E_{\rm max} \ll 10^2$ PeV, because of the kinematic threshold for this channel. Finally, for some massive winds characterized by $\dot{M} \gg 10\ {\rm M}_\odot\ {\rm yr}^{-1}$, the gamma-ray emission from the wind might become comparable with the SBN component even below the TeV range.

4.2 Exploring the parameter space

In the discussion above we identified two main prototypical examples of SBGs, but clearly the zoo of these astrophysical objects cannot be reduced to just two cases. Here we provide a brief overview of what is expected to happen in different realizations of such systems. We do so by exploring a grid of different configurations of the main macroscopic wind properties, mass-loss rate ($\dot{M}$), and terminal wind speed (V_∞), and later by focusing on some specific parameter variations and the associated outcome. The corresponding relevant quantities are summarized in two pairs of plots (Figs 4 and 5) and in Table 2. In what follows we focus on the effects of different conditions on (1) maximum energy and (2) luminosity.

In our parameter investigation we define a range for the mass-loss rate, $0.1 < \dot{M}/({\rm M}_\odot\ {\rm yr}^{-1}) < 50$, and for the terminal wind speed, $0.5 < V_\infty/(10^3\ {\rm km\ s}^{-1}) < 3$. In order to keep track of the temporal evolution, we additionally select two characteristic times at which we take a snapshot of the system: $T_{\rm age,1} = 100$ Myr and $T_{\rm age,2} = 250$ Myr. In Figs 4 and 5, we show the results obtained at $T_{\rm age,1}$ and $T_{\rm age,2}$, respectively, under the assumption of $P_{\rm h}/k_{\rm B} = 5 \times 10^4\ {\rm K\ cm}^{-3}$. The upper panels illustrate the changes in the maximum energy $E_{\rm max}$ and the lower panels show the single flavour neutrino flux at 25 TeV, $\tilde{F}_{\nu_\mu}$. In general, it can be observed that the higher the power of the system ($\dot{M}V_\infty^2$), the higher the maximum energy. In particular, as discussed in Section 3 (see also MBPC21, for additional details), the most stringent condition on the maximum energy is typically set by the transport in the upstream region as $D(E^{(1)}_{\rm max}) = R_{\rm sh} V_\infty$. Such a

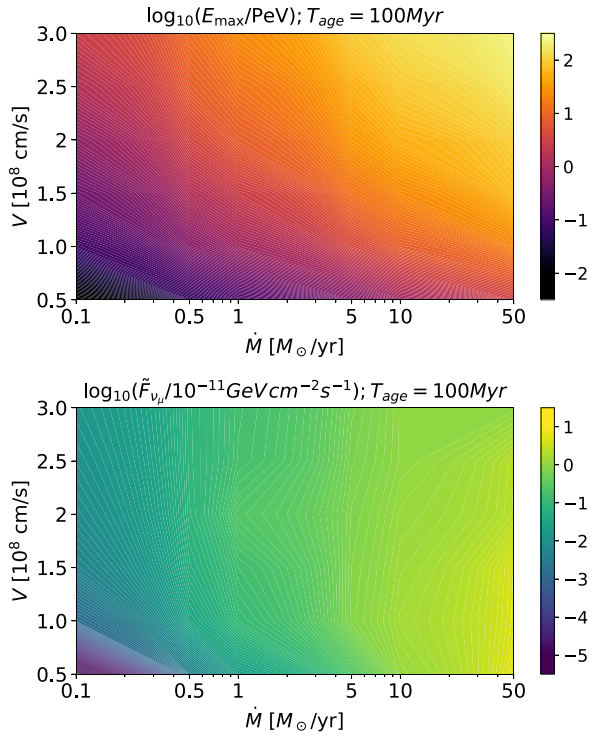

Figure 4. Contour plots illustrating the parameter space ($\dot{M}$, V_∞) exploration based on different realizations of the system at the age $T_{\rm age,1} = 100$ Myr. The associated colour code is shown at the right of each panel. Top panel: maximum energy normalized to 1 PeV. Bottom panel: single flavour neutrino flux at 25 TeV.

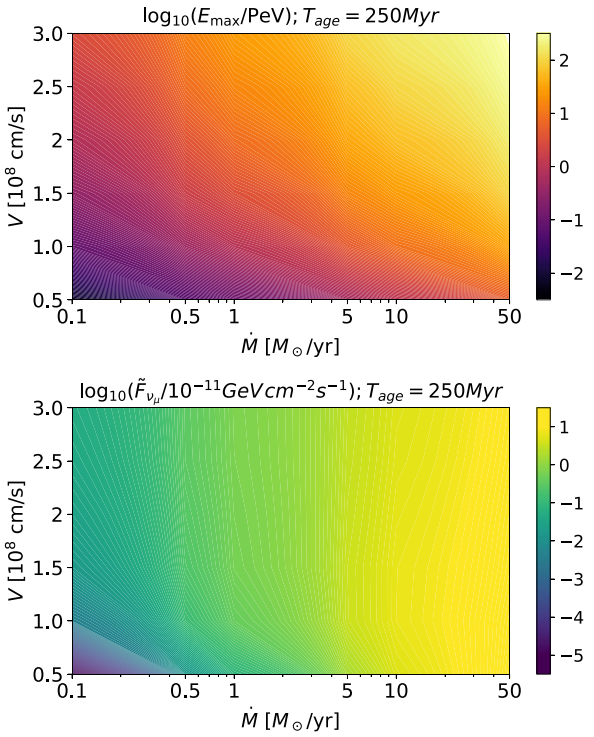

Figure 5. Contour plots illustrating the parameter space ($\dot{M}$, V_∞) exploration based on different realizations of the system at the age $T_{\rm age,2} = 250$ Myr. Top and bottom panels are the same as in Fig. 4.

condition can be re-expressed as

$$E^{(1)}_{\rm max} = \dot{M}^{1/[2(2-\delta)]} V_\infty^{3/[2(2-\delta)]} \frac{q_{\rm e}\,\epsilon_{\rm B}^{1/2}\left[3\,l_{\rm c}^{(1-\delta)}\,c^{-1}\right]^{1/(2-\delta)}}{(4\pi P_{\rm h})^{(\delta-1)/[2(2-\delta)]}}, \qquad (19)$$

which leads to $E^{(1)}_{\rm max} \propto \dot{M} V_\infty^3$ for the assumed Kraichnan-like turbulence. Notice that although the maximum energy in equation (19) identifies an energy where the flux drops most prominently, as discussed above, the spherical symmetry of the problem leads to a gradual spectral steepening at energies below $E_{\rm max}$. This effect is embedded in the two functions Γ_1 and Γ_2 described in Section 3. At odds with the case of the maximum energy, the neutrino luminosity has a very mild dependence on the terminal wind speed provided that it is above the threshold to accelerate efficiently >PeV particles, whereas it has approximately a linear dependence on the mass-loss rate. The latter scaling is due to the direct connection between $\dot{M}$ and the target density.

By comparing the results obtained at $T_{\rm age,1}$ with those obtained at $T_{\rm age,2}$ we observe that the age of the system does not have a dominant impact on the maximum energy as expected from equation (19): the acceleration time is much shorter than the dynamical time of these systems. The slight difference can be understood by the interplay between the two functions, Γ_1 and Γ_2 regulating the HE cut-off. In fact, an older system is characterized by a less stringent constraint produced by Γ_2, while the one set by Γ_1 is practically unmodified. On the other hand the luminosity is found to increase with time due to the increase of target material accumulated in the downstream region.

Table 2. Different scenarios considered. The physical units are the same as in Table 1. For the case P3 the wind bubble is not pressure confinement and different equations are used to estimate the bubble properties.

	L1	L2	P1	P2	P3	T1	T2
$\dot{M}$	20	2	5	5	5	5	5
V_∞	3	1	2	2	2	2	2
$P_{\rm h}/k_{\rm B}$	2.5	2.5	10	0.5	0.01	2.5	2.5
$t^*_{\rm age}$	250	250	250	250	250	100	300
$R_{\rm sh}$	30	5.5	6	28	40	12	12
$R_{\rm FS}/R_{\rm sh}$	2.5	5.5	6.7	2.5	2	2.2	4.3
$E_{\rm max}$	225	2	26	59	58	34	44
$\tilde{F}_{\nu_\mu}$	2.6	0.45	8.7	0.15	0.06	0.24	1.5

In order to evaluate the impact of changing other relevant parameters' values, we now focus on a set of limited cases listed in Table 2 and discuss quantitatively their numerical outcomes. We first change the total luminosity of the system: L1 corresponds to a strong wind as the one that can be found in LIRGs; L2 corresponds to a mild star-forming source. In line with what we discussed above, these two situations illustrate that, maintaining the same halo conditions, the maximum energy increases with the power of the wind. The location of the wind termination shock and of the forward shock is moved farther away from the centre when the power is larger. Consequently, the most powerful sources naturally lead to a larger volume of the bubble and higher gamma-ray and neutrino luminosity.

In scenarios P1, P2, and P3, the total power is as in B0, but the surrounding pressure in the halo varies by three orders of magnitude. This again impacts the location of the termination shock $R_{\rm sh}$ that in

turn affects the maximum energy even though this latter quantity varies only by a factor of ∼2. In particular, in agreement with equation (19), the smaller the halo pressure, the higher the maximum energy. Although equation (19) is informative on the dependence of the maximum energy on the CGM pressure, the actual scaling of $E_{\rm max}$ on $P_{\rm h}$ is not straightforward due to the role played by the functions Γ_1 and Γ_2 in shaping the spectrum close to $E_{\rm max}$, and due to the transition of the diffusion coefficient to the $\sim E^2$ regime, when $r_{\rm L} \approx L_{\rm c}$. The last effect is in fact occurring at energies close to the actual $E_{\rm max}$. Scenario P3 corresponds to a relatively extreme situation since the wind evolves in a very low pressure environment compared to what might be expected in a starburst halo. Under these conditions, the system would need ∼5 Gyr to reach the pressure-confined state. Consequently, both the forward and the wind shocks are still in their expansion phase after 250 Myr. In this case, the wind shock radius cannot be computed under the pressure-confined assumption, so that we adopt equation (4.2) of Koo & McKee (1992a). In this scenario the maximum energy is somewhat close to the scenario labelled as P2, but the luminosity is smaller due to the lower ram pressure at the shock that, in turn, results from the larger shock distance from the centre. Even if the impact on the maximum energy is marginal, the value of the circumgalactic pressure strongly impacts on the gamma-ray and neutrino luminosity. This is a direct consequence of the assumed proportionality between the CR energy density and the free wind ram pressure that is, in turn, roughly equal to the external pressure. Comparing cases P1 with P3, where $P_{\rm h}$ is 10^3 smaller, the neutrino luminosity decreases by ∼140 times. The proportionality is not exactly linear because the spatial distribution of both CRs and gas in the two cases is different.

By comparing scenario L2 with P1 and L1 with P2, one can notice that sources with similar age and size can strongly differ both in maximum energy and luminosity. The former result can be easily understood given the dependence of the maximum energy on the V_∞ (see equations 15, 16, and 19). The luminosity, on the other hand, is set by the combination of the pressure at the shock, which determines the total number of accelerated particles, and the target density (which in turn depends on $\dot{M}$).

Finally, T1 and T2 correspond to B0 at different times $t_{\rm age}$, 100 and 300 Myr, illustrating that the slow evolution in time of the system does not have a strong impact on the maximum energy. However, sources become more luminous while ageing, due to the target material that accumulates and larger volume of the shocked-wind region where pp interactions are taking place. This supports numerically what has been discussed above based upon the contour plots parameter investigation.

5 DIFFUSE FLUXES OF COSMIC RAYS, GAMMA-RAYS, AND NEUTRINOS

In this section, we illustrate our calculations of the diffuse flux of gamma-rays, neutrinos, and cosmic rays (CRs) due to the collective emission of starburst galactic winds distributed in redshift. In Section 5.1, we evaluate the starburst contribution to the diffuse fluxes of gamma-rays and neutrinos and compare them to those observed by *Fermi*-LAT (Ackermann et al. 2015) and IceCube (Abbasi et al. 2021), respectively. In Section 5.2, we explore the associated flux of CR protons accelerated at the termination shock and eventually escaping the bubble.

5.1 Gamma-rays and neutrinos

We work under the assumption that starburst winds are ubiquitous in SBGs and we count sources following the star formation rate function (SFRF) approach previously adopted by Peretti et al. (2020) and defined for redshift up to $z = 4.2$ (see also Gruppioni et al. 2015, for additional details). Differently from the case of SBNs, where, as discussed by Peretti et al. (2020), the luminosity scales with the SFR, the dependence of the wind properties on the SFR is highly non-trivial and difficult to constrain. Therefore, in the following we rely on the assumption that on average all winds above a given SFR value, $\psi_{\rm min}$, can be described in terms of a single prototype. The diffuse flux can be computed as

$$\Phi_j(E) = \frac{1}{4\pi}\int \mathrm{d}\Omega \int_0^{4.2} \mathrm{d}z\, \frac{\mathrm{d}V_{\rm C}(z)}{\mathrm{d}z\,\mathrm{d}\Omega}\, \mathrm{e}^{-\tau_j(E,z)} \times \int_{\psi_{\rm min}}^{\infty} \mathrm{d}\log\psi\ \Phi_{\rm SFR}(\psi, z)\,[1+z]^2 f_j(E[1+z], \psi), \tag{20}$$

where $f_j(E,\ \psi)$ is the flux density of the particle specie $j = \{\gamma,\ \nu\}$, $\Phi_{\rm SFRF}$ is the SFRF, and $\mathrm{d}V_{\rm C} = cD_{\rm C}^2(z)/[E(z)\,H_0]\,\mathrm{d}z\,\mathrm{d}\Omega$ is the comoving volume element per redshift interval $\mathrm{d}z$ and solid angle $\mathrm{d}\Omega$. In a spatially flat space–time $D_{\rm C}(z) = D_{\rm L}(z)/(1+z)$ and $E(z) = \sqrt{\Omega_{\rm M}(1+z)^3 + \Omega_\Lambda}$. The quantity τ_j is assumed to vanish in the neutrino case, while in the case of gamma-rays, it represents the opacity due to the presence of the EBL and cosmic microwave background (CMB) (Franceschini & Rodighiero 2017). The contribution of the electromagnetic cascade is computed as in Peretti et al. (2020) (see also Berezinsky & Kalashev 2016, for additional details). Finally, $\psi_{\rm min}$ represents the minimum SFR that we adopt as a free parameter considering the value of $\psi^* \sim 1\,{\rm M}_\odot\,{\rm yr}^{-1}$ (Peretti et al. 2020) as a firm lower limit. The assumption of $\psi_{\rm min}$ as free parameter is dictated by the poorly constrained ratio between the mass-loss rate of the wind and the SFR in the SBN, $\mathcal{R} = \dot{M}/{\rm SFR}$ (see e.g. Veilleux et al. 2005, for a detailed discussion). In general $\mathcal{R} \lesssim 2$ (see also Bustard et al. 2016; Zhang 2018, for detailed discussions), hence we fix $\mathcal{R} = 2$. Therefore, $\psi_{\rm min}$ increases with the wind mass-loss rate.

We calculate the diffuse emission from the SBN and from its wind in two scenarios, which we refer to here as I and II, in which B0 and B1 are respectively used as a prototype (see Table 1). Following our criterion on $\mathcal{R}$, we adopt a $\psi_{\rm min}$ of 2.5 and 5 ${\rm M}_\odot\,{\rm yr}^{-1}$ for cases I and II, respectively.

In Fig. 6, we show the spectra of diffuse gamma-rays and ν_μ for the two scenarios I and II (top and bottom panels, respectively). In both cases the central SBN provides the main contribution to the total gamma-ray diffuse flux (dashed violet line and thick red line, respectively). The latter lies below the diffuse flux measured by *Fermi*-LAT and never exceeds the upper limits imposed by the superposition of point-like sources (e.g. Lisanti et al. 2016). As described above, the wind region also contributes to the gamma-ray emission, and the corresponding diffuse flux is shown as an orange two-dot–dashed line in Fig. 6. The cascade components (three-dot–dashed brown and dot–dashed magenta for SBNs and winds, respectively) are always subdominant and change their relative contribution depending on the scenario.

The neutrino flux from SBNs (empty green circles) drops considerably above ∼50 TeV, as a result of the proton maximum energy at sources in the SBN being ∼1 PeV. The flux of neutrinos produced in the wind (empty grey triangles) through pp collisions extends to $\gtrsim$300 TeV and dominates the diffuse emission at such energies, at least at the level of $\sim 10^{-9}$ GeV cm^{-2} s^{-1} sr^{-1} in the most pessimistic scenario (case I) (this lower limit corresponds to ∼10 per cent of the IceCube flux of through-going muons reported by Haack & Wiebusch 2017). We finally notice that if star-forming galaxies were dominating the diffuse gamma-ray flux as suggested by Linden (2017) and Roth

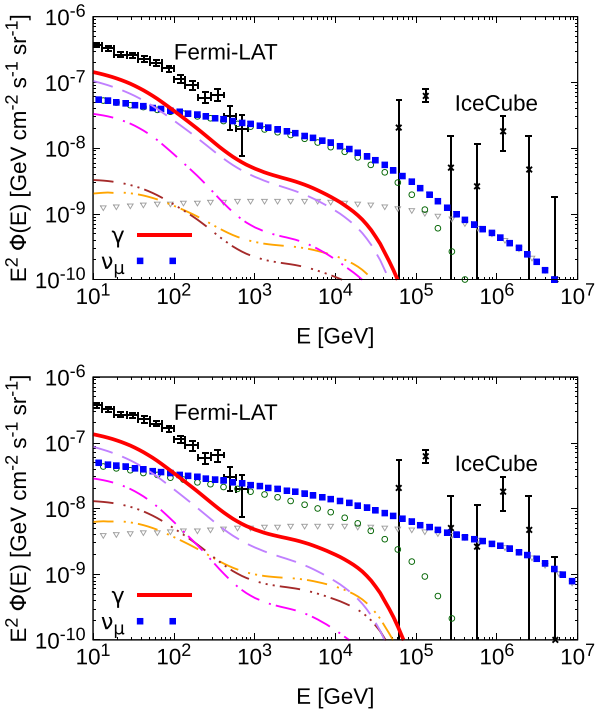

Figure 6. Multimessenger emission for scenarios I and II (top and bottom panels, respectively) compared with *Fermi*-LAT (Ackermann et al. 2015) and IceCube (Abbasi et al. 2021) data. The colour code is the same for all panels: total gamma-rays and single flavour neutrinos are shown as thick red lines and blue filled squares, respectively. Direct gamma-ray component from the SBN and wind (dashed violet and two-dot–dashed orange, respectively) are shown separately with their associated cascade spectra (dot–dashed magenta and three-dot–dashed, respectively). The neutrino components from SBNs (green empty circles) and from the winds (grey empty triangles) are shown separately.

et al. (2021), the associated neutrino flux would correspondingly increase.

5.2 Cosmic rays

Cosmic ray (CR) protons accelerated at the termination shock of the SBG wind eventually escape the system from the outer edge of the bubble. Since energy losses do not affect the spectrum of these particles in a significant way, the escape spectrum is similar to the spectrum of particles accelerated at the termination shock. The diffuse flux of protons contributed by SBG winds, calculated using equation (20) that neglects any propagation effects due to the intergalactic magnetic fields, is shown in Fig. 7 for the scenarios I and II introduced earlier. Notice that since the maximum energy of accelerated particles is $\lesssim$few hundred PeV, below the threshold for Bethe–Heitler pair production, the transport of these CRs on cosmological scales is dominated by adiabatic losses alone as due to the expansion of the Universe. In Fig. 7, the predicted proton fluxes are compared with data of the all-particle spectrum and on the light component alone, as collected by IceTop (Aartsen et al. 2019), Tunka (Epimakhov et al. 2013; Prosin et al. 2016), and KASCADE–Grande (Arteaga-Velázquez et al. 2017). This shows that if indeed particle acceleration at winds termination shock does take place, so as to contribute to the HE neutrino flux, a sizeable contribution

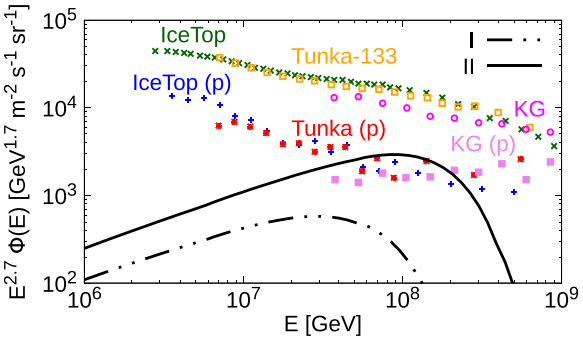

Figure 7. Diffuse proton flux escaped from the starburst wind and propagated to the Earth for the prototype cases B0 (dot–dot–dashed) and B1 (thick). The predicted proton flux is compared with data from Tunka (Epimakhov et al. 2013; Prosin et al. 2016), KASCADE–Grande (Arteaga-Velázquez et al. 2017), and IceTop (Aartsen et al. 2019).

to the protons CR flux measured at the Earth should be expected. Notice that here we only estimated the flux of protons from SBGs, but it is reasonable to expect that heavier nuclei are also accelerated, if present in the wind. Such nuclei would contribute to the total CR flux at higher energies. We also observe that our results on the starburst contribution to the CR spectrum are qualitatively supported by Zhang, Murase & Mészáros (2020) where, however, different assumptions were adopted for both the acceleration and transport of HE particles in galactic winds.

A comment on the spectral shape of CRs from SBGs is in order: one can see in Fig. 7 that the spectrum expected at the Earth is similar to that originated at individual wind bubbles, as a consequence of the fact that adiabatic losses do not change the spectral shape. On the other hand, such a straightforward connection can be made here only because of the assumption that all SBGs can be considered as similar to one of the two prototypical sources adopted here. In general this is not the case, and one should expect that the higher the wind luminosity, the higher the maximum energy of the accelerated particles, but the lower the number of such objects in the Universe. As a result, qualitatively, one might expect that the diffuse flux of CR protons (as well as neutrinos) might become steeper at energies higher than the maximum energy associated with the least luminous of the winds, as discussed in a generic case by Kachelrieß & Semikoz (2006). We finally observe that, based on our calculations, it is difficult to accelerate protons above $\sim 10^{18}$ eV in the wind of normal SBGs.

6 DISCUSSION AND CONCLUSION

The theory of particle acceleration at the termination shock of winds originating in star clusters, as developed by Morlino et al. (2021), has been adapted here to the description of particle acceleration at the termination shock of starburst winds. At such shock the wind from the SBN is slowed down and heated up, so as to reach approximate pressure balance with the galactic halo in which the wind was originally expanding. In fact a weak forward shock moves slowly through the halo medium, but its Mach number is too low to be of relevance for particle acceleration.

We have assumed a stationary spherical geometry for the wind-blown bubble. Even though numerical simulations might show a variety of possible deviations from such an assumption, particle acceleration and transport are not particularly affected by such

details. The theoretical approach is used to calculate the spectrum of accelerated particles and their spatial distribution inside the wind bubble, as well as their escape flux from the edge of the bubble. We discussed two prototypical SBG models, assumed to represent, respectively, a galaxy like M82 or NGC 253 and a LIRG, and for each the flux of gamma-rays and neutrinos produced due to CR interactions in the SBN and in the wind bubble has been calculated. The absorption of the gamma-rays both inside the nucleus and en route to the Earth has been taken into account.

The maximum energy of accelerated particles at the termination shock varies between a few tens PeV and 200 PeV for the two prototypes of SBGs considered here and in a range from a few PeV up to a few hundred PeV exploring a wider range of parameters. This implies that the corresponding neutrino flux extends up to 1–10 PeV, while the neutrino flux from the SBN is expected to extend up to a few tens of TeV, if CRs are accelerated by SNRs as in the Milky Way. Given the fact that the termination shock is strong, for the parameters adopted here, the spectrum of accelerated particles at $E \ll E_{\rm max}$ is close to p^{-4}. Some theoretical arguments can be put forward, for instance based on a finite velocity of scattering centres in the downstream region, to argue that slightly steeper spectra are possible (see e.g. Caprioli et al. 2020).

The diffuse gamma-ray flux due to the superposition of SBGs is dominated by the contribution of the central SBNs for energies $\lesssim$1 TeV. This flux does not exceed the upper limits imposed by *Fermi*-LAT based on the contribution of point-like sources (e.g. Lisanti et al. 2016). The wind region also contributes to the gamma-ray emission and such contribution can become comparable with that of the SBNs for $E \gtrsim 1$ TeV, if the more luminous prototype is adopted in the calculation of the diffuse flux. The neutrino flux from SBNs drops considerably above $\sim$50 TeV, as a result of the proton maximum energy at sources in the SBN. On the contrary, the flux of neutrinos produced in the wind through pp collisions extends to $\gtrsim$300 TeV and dominates the diffuse emission at such energies. The diffuse flux in this energy region is compatible with the IceCube data.

The observational confirmation that particle acceleration at the termination shock and production of gamma-rays and neutrinos in the wind bubble do take place can be achieved to some extent with upcoming observational facilities, as we discuss below. The study of starburst-driven galactic winds is generally performed via atomic and molecular line shifts and measurements of the X-ray luminosity (Veilleux et al. 2005; Strickland & Heckman 2009), but so far, detection in the gamma-ray domain is rather limited, and unable to resolve the SBN emission from a possible contribution from the wind bubble. A gamma-ray survey would be ideal to probe the model discussed in this work and would provide key information on its acceleration properties and luminosity. However, the most useful information would come from direct detection of the gamma-ray emission from the wind region. In the very high energy range, the nearest starbursts, M82 and NGC 253, could already be resolved by current instruments. In fact, a bubble of size $\sim$50 kpc, at a distance of $\sim$3–4 Mpc, corresponds to an angular size $\theta \sim 1^\circ$, typically resolved by Imaging Air Cherenkov Telescopes (IACTs; Aleksić et al. 2016; Park 2016; Zorn 2019). However, given the total volume integrated luminosity of the order of $L_\gamma(10\,{\rm TeV}) \sim 10^{41}$ GeV s^{-1}, expected for these sources, this task remains challenging.

Next generation IACTs, such as Astrofisica con Specchi a Tecnologia Replicante Italiana (ASTRI) and Cherenkov Telescope Array (CTA), with improved angular resolution and sensitivity, will open promising perspectives for a morphological study of these sources (Vercellone 2016; Cherenkov Telescope Array Consortium et al. 2019). A second method for probing the gamma-ray emission of the starburst wind consists in a spectral detection of the source at energy $E \gtrsim 10$ TeV. The main reason for that is because gamma–gamma absorption on the infrared (IR) is expected to be important above a few TeV in the SBNs. Differently, the emission from the wind comes basically unabsorbed. The observation of non-thermal radio/X-ray emission at large distances from the galactic disc can also be adopted to trace both the acceleration of primary electrons and the presence of secondaries produced via pp and pγ interactions. A multiwavelength modelling focused on the leptonic emission is left for future investigation.

The detectability of SBGs as isolated neutrino sources is disfavoured for the standard parameters adopted in this work. However, very young systems or scenarios involving high mass-loss rates, $\dot{M} \gtrsim 10\,{\rm M}_\odot\,{\rm yr}^{-1}$, can possibly produce fluxes close to the sensitivity level of km^2 detectors (Aiello et al. 2019; Aartsen et al. 2021). Differently from a single isolated source, the combined contribution of SBGs might provide interesting indications with higher statistical significance.

Finally, we checked that the flux of CR protons accelerated at the termination shock and eventually propagating to the Earth is not in conflict with present day observation of the protons spectrum. In fact the diffuse flux of CRs from starburst wind bubbles is tantalizingly close to the observed flux, and limited to energies $\lesssim$a few hundreds PeV, although it cannot be excluded that ultraluminous SBGs or SBG with AGN activity may lead to the production of CRs with somewhat larger energies.

However, the role of SBGs in contributing to the observed CR flux at $\sim 10^{17}$ eV needs some additional support to be more robust than an order of magnitude estimation. Finally, in the context of the model developed in this work, we do not expect regular starbursts to be able to produce protons at energies larger than a few hundred PeV. We cannot exclude that higher energies may be reached in galaxies with starburst activity hosting AGN jets, where particle acceleration would be regulated by different physical processes.

ACKNOWLEDGEMENTS

This project has received funding from the European Union's Horizon 2020 Framework Programme under the Marie Sklodowska-Curie grant agreement no. 847523 'INTERACTIONS'. The research activity of EP was partially supported by Villum Fonden (project no. 18994). The research activity of PB and GM was partially funded through support Grant ASI/INAF no. 2017-14-H.O; GM was also funded through Grants SKA-CTA-INAF 2016 and INAF-Mainstream 2018. EP is grateful to M. Ahlers, A. Lamastra, and E. M. de Gouveia Dal Pino for useful comments and to O. Pezzi, A. Dundovic, D. Boncioli, S. Petrera, and A. Condorelli for helpful discussions at the initial stage of the work.

DATA AVAILABILITY

No data have been analysed or produced in this work. The phenomenological predictions performed in this work are compared with the data produced and analysed in available publications. In particular, *Fermi*-LAT gamma-ray data can be found in Ackermann et al. (2015) and IceCube neutrino data are published in Abbasi et al. (2021). CR data measured by IceTop, KASCADE–Grande, and Tunka can be found, respectively, in Aartsen et al. (2019), Arteaga-Velázquez et al. (2017), and Epimakhov et al. (2013) and Prosin et al. (2016).

REFERENCES

Aab A. et al., 2018, ApJ, 853, L29
Aartsen M. G. et al., 2019, Phys. Rev. D, 100, 082002
Aartsen M. G. et al., 2021, J. Phys. G: Nucl. Part. Phys., 48, 060501
Abbasi R. et al., 2021, Phys. Rev. D, 104, 022002
Ackermann M. et al., 2012, ApJ, 755, 164
Ackermann M. et al., 2015, ApJ, 799, 86
Aiello S. et al., 2019, Astropart. Phys., 111, 100
Ajello M., Di Mauro M., Paliya V. S., Garrappa S., 2020, ApJ, 894, 88
Aleksić J. et al., 2016, Astropart. Phys., 72, 76
Ambrosone A., Chianese M., Fiorillo D. F. G., Marinelli A., Miele G., Pisanti O., 2021a, MNRAS, 503, 4032
Ambrosone A., Chianese M., Fiorillo D. F. G., Marinelli A., Miele G., 2021b, ApJ, 919, L32
Anchordoqui L. A., 2018, Phys. Rev. D, 97, 063010
Anchordoqui L. A., Romero G. E., Combi J. A., 1999, Phys. Rev. D, 60, 103001
Anderson M. E., Churazov E., Bregman J. N., 2016, MNRAS, 455, 227
Arteaga-Velázquez J. C. et al., 2017, PoS, ICRC2017, 316
Bechtol K., Ahlers M., Di Mauro M., Ajello M., Vandenbroucke J., 2017, ApJ, 836, 47
Berezhko E. G., Völk H. J., 1997, Astropart. Phys., 7, 183
Berezinsky V., Kalashev O., 2016, Phys. Rev. D, 94, 023007
Blasi P., 2013, A&AR, 21, 70
Blasi P., Amato E., 2019, Phys. Rev. Lett., 122, 051101
Bolatto A. D. et al., 2013, Nature, 499, 450
Breitschwerdt D., McKenzie J. F., Voelk H. J., 1991, A&A, 245, 79
Buckman B. J., Linden T., Thompson T. A., 2020, MNRAS, 494, 2679
Bustard C., Zweibel E. G., D'Onghia E., 2016, ApJ, 819, 29
Bustard C., Zweibel E. G., Cotter C., 2017, ApJ, 835, 72
Capanema A., Esmaili A., Serpico P. D., 2021, J. Cosmol. Astropart. Phys., 02, 037
Caprioli D., Haggerty C. C., Blasi P., 2020, ApJ, 905, 2
Carilli C. L., 1996, A&A, 305, 402
Castor J., McCray R., Weaver R., 1975, ApJ, 200, L107
Cherenkov Telescope Array Consortium et al., 2019, Science with the Cherenkov Telescope Array. World Scientific Press, Singapore
Chevalier R. A., Clegg A. W., 1985, Nature, 317, 44(CC85)
Cicone C. et al., 2014, A&A, 562, A21
Cooper J. L., Bicknell G. V., Sutherland R. S., Bland-Hawthorn J., 2007, Ap&SS, 311, 99
Di Matteo P., Bournaud F., Martig M., Combes F., Melchior A. L., Semelin B., 2008, A&A, 492, 31
Dorfi E. A., Breitschwerdt D., 2012, A&A, 540, A77
Dundovic A., Pezzi O., Blasi P., Evoli C., Matthaeus W. H., 2020, Phys. Rev. D, 102, 103016
Epimakhov S. et al., 2013, in Saa A., ed., 33rd International Cosmic Ray Conference (ICRC2013). Brazilian Physical Society, São Paulo, Brazil, p. 818
Everett J. E., Zweibel E. G., Benjamin R. A., McCammon D., Rocks L., Gallagher John S. I., 2008, ApJ, 674, 258
Fielding D., Quataert E., Martizzi D., Faucher-Giguère C.-A., 2017, MNRAS, 470, L39
Fielding D., Quataert E., Martizzi D., 2018, MNRAS, 481, 3325
Förster Schreiber N. M. et al., 2001, ApJ, 552, 544
Franceschini A., Rodighiero G., 2017, A&A, 603, A34
Galliano F., Dwek E., Chanial P., 2008, ApJ, 672, 214
Gao Y., Solomon P. M., 2004, ApJ, 606, 271
Girichidis P., Pfrommer C., Pakmor R., Springel V., 2022, MNRAS, 510, 3917
Gruppioni C. et al., 2015, MNRAS, 451, 3419
Haack C., Wiebusch C., 2017, PoS, ICRC2017, 1005
Hanasz M., Lesch H., Naab T., Gawryszczak A., Kowalik K., Wóltański D., 2013, ApJ, 777, L38
H. E. S. S. Collaboration et al., 2018, A&A, 617, A73
IceCube Collaboration et al., 2013, Science, 342, 1242856
Kachelrieß M., Semikoz D. V., 2006, Phys. Lett. B, 634, 143
Kafexhiu E., Aharonian F., Taylor A. M., Vila G. S., 2014, Phys. Rev. D, 90, 123014
Kelner S. R., Aharonian F. A., 2008, Phys. Rev. D, 78, 034013
Kelner S. R., Aharonian F. A., Bugayov V. V., 2006, Phys. Rev. D, 74, 034018
Kennicutt R. C., Jr, 1998, ARA&A, 36, 189
Koo B.-C., McKee C. F., 1992a, ApJ, 388, 93
Koo B.-C., McKee C. F., 1992b, ApJ, 388, 103
Kornecki P., Pellizza L. J., del Palacio S., Müller A. L., Albacete-Colombo J. F., Romero G. E., 2020, A&A, 641, A147
Kornecki P., Peretti E., del Palacio S., Benaglia P., Pellizza L. J., 2022, A&A, 657, A49
Krumholz M. R., Crocker R. M., Xu S., Lazarian A., Rosevear M. T., Bedwell-Wilson J., 2020, MNRAS, 493, 2817
Lamastra A. et al., 2016, A&A, 596, A68
Lamastra A., Tavecchio F., Romano P., Landoni M., Vercellone S., 2019, Astropart. Phys., 112, 16
Linden T., 2017, Phys. Rev. D, 96, 083001
Lisanti M., Mishra-Sharma S., Necib L., Safdi B. R., 2016, ApJ, 832, 117
Liu R.-Y., Murase K., Inoue S., Ge C., Wang X.-Y., 2018, ApJ, 858, 9
Lochhaas C., Thompson T. A., Quataert E., Weinberg D. H., 2018, MNRAS, 481, 1873
Loeb A., Waxman E., 2006, J. Cosmol. Astropart. Phys., 05, 003
McQuinn K. B. W., Skillman E. D., Cannon J. M., Dalcanton J. J., Dolphin A., Stark D., Weisz D., 2009, ApJ, 695, 561
Mannucci F. et al., 2003, A&A, 401, 519
Melioli C., de Gouveia Dal Pino E. M., Geraissate F. G., 2013, MNRAS, 430, 3235
Merten L., Bustard C., Zweibel E. G., Becker Tjus J., 2018, ApJ, 859, 63
Morlino G., Blasi P., Peretti E., Cristofari P., 2021, MNRAS, 504, 6096(MBPC21)
Müller A. L., Romero G. E., Roth M., 2020, MNRAS, 496, 2474
Murase K., Guetta D., Ahlers M., 2016, Phys. Rev. Lett., 116, 071101
Murase K., Kimura S. S., Mészáros P., 2020, Phys. Rev. Lett., 125, 011101
Palladino A., Fedynitch A., Rasmussen R. W., Taylor A. M., 2019, J. Cosmol. Astropart. Phys., 09, 004
Papadopoulos P. P., Thi W.-F., Miniati F., Viti S., 2011, MNRAS, 414, 1705
Park N., 2016, PoS, ICRC2015, 771
Peng F.-K. et al., 2016, ApJ, 821, L20
Peretti E., Blasi P., Aharonian F., Morlino G., 2019, MNRAS, 487, 168
Peretti E., Blasi P., Aharonian F., Morlino G., Cristofari P., 2020, MNRAS, 493, 5880
Pfrommer C., Pakmor R., Simpson C. M., Springel V., 2017, ApJ, 847, L13
Prosin V. V. et al., 2016, EPJ Web Conf., 121, 03004
Recchia S., Blasi P., Morlino G., 2016, MNRAS, 462, 4227
Recchia S., Gabici S., Aharonian F. A., Niro V., 2021, ApJ, 914, 135
Romero G. E., Müller A. L., Roth M., 2018, A&A, 616, A57
Roth M. A., Krumholz M. R., Crocker R. M., Celli S., 2021, Nature, 597, 341
Schneider E. E., Ostriker E. C., Robertson B. E., Thompson T. A., 2020, ApJ, 895, 43
Strickland D. K., Heckman T. M., 2009, ApJ, 697, 2030
Strickland D. K., Stevens I. R., 2000, MNRAS, 314, 511
Strickland D. K., Heckman T. M., Weaver K. A., Hoopes C. G., Dahlem M., 2002, ApJ, 568, 689
Subedi P. et al., 2017, ApJ, 837, 140
Sudoh T., Totani T., Kawanaka N., 2018, PASJ, 70, 49
Tamborra I., Ando S., Murase K., 2014, J. Cosmol. Astropart. Phys., 09, 043
Taylor A. M., Gabici S., Aharonian F., 2014, Phys. Rev. D, 89, 103003
Tenorio-Tagle G., Muñoz-Tuñón C., 1997, ApJ, 478, 134
Thompson T. A. et al., 2006, ApJ, 645, 186
Tumlinson J., Peeples M. S., Werk J. K., 2017, ARA&A, 55, 389
Veilleux S., Cecil G., Bland-Hawthorn J., 2005, ARA&A, 43, 769
Vercellone S., 2016, EPJ Web Conf., 121, 04006
Wang X., Loeb A., 2017, Phys. Rev. D, 95, 063007
Weaver R., McCray R., Castor J., Shapiro P., Moore R., 1977, ApJ, 218, 377
Werhahn M., Pfrommer C., Girichidis P., Winner G., 2021, MNRAS, 505, 3295

Westmoquette M. S., Smith L. J., Gallagher J. S. I., Trancho G., Bastian N., Konstantopoulos I. S., 2009a, ApJ, 696, 192
Westmoquette M. S., Gallagher J. S., Smith L. J., Trancho G., Bastian N., Konstantopoulos I. S., 2009b, ApJ, 706, 1571
Wik D. R. et al., 2014, ApJ, 797, 79
Williams P. K. G., Bower G. C., 2010, ApJ, 710, 1462
Yoast-Hull T. M., Everett J. E., Gallagher J. S., Zweibel E. G., 2013, ApJ, 768, 53
Zhang D., 2018, Galaxies, 6, 114
Zhang Z., Murase K., Mészáros P., 2020, MNRAS, 492, 2250
Zirakashvili V., Völk H., 2006, Adv. Space Res., 37, 1923
Zorn J., 2019, PoS, ICRC2019, 834

APPENDIX A: ESTIMATES OF TIME-SCALES AND LUMINOSITY OF THE SHOCKED BUBBLE

The order of magnitude of the wind-bubble luminosity can be estimated in a simplified way from the total power of the system and the dominant time-scales. The dominant escape time from the system is the advection that reads

$$\tau_{\rm adv} \approx \frac{R_{\rm esc}}{\langle v_2 \rangle} \approx 10^2\, R_{\rm FS,1} u_{1,3}^{-1}\,{\rm Myr}, \tag{A1}$$

where $\langle v_2 \rangle \sim u_2/3$ is the average wind speed in the downstream region and $R_{\rm FS,1}$ is the forward shock location in units of 10 kpc.

The loss time-scales for pp and pγ collisions are described by the following expressions:

$$\tau_{\rm pp} = [\xi_{\rm pp}\, n_2\, \sigma_{\rm pp}\, c]^{-1} \approx 4 \times 10^3\, n_{2,-2}^{-1}\,{\rm Myr}, \tag{A2}$$

$$\tau_{\rm p\gamma} = [\xi_{\rm p\gamma}\, n_{\rm ph}\, \sigma_{\rm p\gamma}\, c]^{-1} \approx 10^3\, U_{\rm OPT,3}^{-1}\, \chi_1^{-2}\,{\rm Myr}, \tag{A3}$$

where we assumed that the target photon field is a Dirac-δ at 1 eV and where $\chi = R_{\rm SBN}/R_{\rm sh}$, while $\xi_{\rm pp} \sim 0.1$ and $\xi_{\rm p\gamma} \sim 0.2$ are the elasticity factors.

Since $\tau_{\rm adv} \ll \tau_{\rm loss}$ one concludes that the dynamical relevance of losses is negligible, so that the assumption of negligible energy losses is fully justified in the shocked wind.

Since the advection dominates, the CR distribution function is approximately constant in the whole shocked bubble. Assuming now that the luminosity of accelerated particles is a fraction $\xi_{\rm CR}$ of the total wind power $\dot{E} = \dot{M}\, u_1^2/2$, we can express the gamma-ray luminosity as

$$L_\gamma \approx \frac{\xi_{\rm CR}}{2} \dot{M}\, u_1^2\, \frac{R_{\rm esc}}{\langle v_2 \rangle}\, n_2 \sigma_{\rm pp} c \xi_{\rm pp}, \tag{A4}$$

which converted in units of standard parameters can be rewritten as

$$L_\gamma \approx 2 \times 10^{40}\, \dot{M}_1\, u_{1,8}\, R_{\rm FS,1}\, n_{2,-2}\, \xi_{\rm CR,-1}\,{\rm erg\,s^{-1}}. \tag{A5}$$

Interestingly, such a value is a fraction $\gtrsim$10 per cent of the luminosity of an SBN when a supernova rate of 0.1 yr^{-1} and perfect calorimetric conditions are assumed. Indeed, under these conditions, the nucleus luminosity in gamma-rays can be written as

$$L_{\rm SBN} \approx \mathcal{R}_{\rm SN} \xi_{\rm CR} E_{\rm SN} \approx 1.6 \times 10^{41}\, \mathcal{R}_{\rm SN,-1}\, \xi_{\rm CR,-1}\, E_{\rm SN,51}. \tag{A6}$$

However, differently from the SBN, the gamma-ray luminosity of the bubble increases with time.

APPENDIX B: ENERGY LOSS FUNCTIONS FOR ACCELERATED PARTICLES IN SPHERICAL GEOMETRY

We report here the analytic expressions of the functions included in the solution presented in Section 3.

The function G_1, embedding the adiabatic energy loss/gain, has the following expression:

$$G_1(r,\, p) = \frac{1}{3} \int_0^r {\rm d}r'\, \tilde{q}(r',\, p)\, f_1(r',\, p)\, \partial_{r'}[r'^2\, u_1(r')], \tag{B1}$$

where $\tilde{q}$ reads

$$\tilde{q}(r,\, p) = -\frac{\partial \ln p^3 f(r,\, p)}{\partial \ln p}. \tag{B2}$$

The function H_1 accounts for pp energy losses and reads

$$H_1(r,\, p) = \int_0^r {\rm d}r'\, r'^2\, f_1(r',\, p)\, n(r')\, \sigma_{\rm pp}(p)\, c, \tag{B3}$$

where $\sigma_{\rm pp}$ is the pp cross-section (see Kelner et al. 2006).

This paper has been typeset from a TEX/LATEX file prepared by the author.